https://doi.org/10.20965/jdr.2024.p0865

Note:

Quality Assessment of Multiple UAV-SfM DEMs Derived for Impact Assessment of a Co-Seismic Avalanche in the Himalayas

Sojiro Sunako[*1,†], Koji Fujita[*2], Satoru Yamaguchi[*1], Hiroshi Inoue[*3], Walter W. Immerzeel[*4], Takeki Izumi[*5], and Rijan B. Kayastha[*6]

[*1]Snow and Ice Research Center, National Research Institute for Earth Science and Disaster Resilience
187-16 Maeyama, Suyoshi, Nagaoka, Niigata 940-0821, Japan
[†]Corresponding author, E-mail: s_sunako667@bosai.go.jp
[*2]Graduate School of Environmental Studies, Nagoya University, Nagoya, Japan
[*3]National Research Institute for Earth Science and Disaster Resilience, Tsukuba, Japan
[*4]Department of Physical Geography, Utrecht University, Utrecht, The Netherlands
[*5]School of Urban Environmental Sciences, Tokyo Metropolitan University, Hachioji, Japan
[*6]Department of Environmental Science and Engineering, School of Science, Kathmandu University, Dhulikhel, Nepal
[Received January 15, 2024; accepted August 1, 2024]

Combined with the structure from motion (SfM) technique, unmanned aerial vehicles (UAVs) are powerful tools for generating high-resolution digital elevation models (DEMs) for application in hazard assessments. During our field observations in October 2015 at Langtang Village, which was destroyed by the Gorkha earthquake in April 2015, three different UAVs with mounted cameras were operated to evaluate the volume of the avalanche deposit covering the village. This study evaluated the performance of DEMs created from the different cameras on board those UAVs. Multiple DEMs for the different cameras, including Sony-α7R (PA7), Ricoh-GR (XGR), and Canon-IXUS (EIX), were created using SfM software. All DEMs were compared with a base DEM created from differential global positioning system survey data, which was obtained simultaneously with the UAV campaigns. The results show that the elevation difference of PA7-, XGR-, and EIX-DEMs are within $\pm$0.14 m; the standard deviations of elevation difference range from 0.33 to 0.40 m. Although there were slightly larger differences in elevation on the southwest-to-west sides of the XGR- and EIX-DEMs, which can be attributed mainly to the flight paths and ground control point network, our DEMs are still of high enough quality to be used in hazard assessments.

Keywords: unmanned aerial vehicle (UAV), digital elevation model (DEM), quality assessment

1. Introduction

Studies adopting unmanned aerial vehicles (UAVs) with the structure from motion (SfM) technique to generate high-resolution digital elevation models (DEMs) and orthomosaics have increased in recent years [1–5]. UAV-based photogrammetry provides advantages such as high mobility and cost-effectiveness compared with conventional ground survey methods, less susceptibility to weather conditions, and higher resolution compared with satellite data. However, in high-elevation regions such as the Himalayas, the use of UAVs with inaccessibility and in thin air is still a significant challenge; thus, only a few UAV studies have been performed [6–11].

On April 25, 2015, the 2015 Gorkha earthquake caused massive avalanches and rockfalls that destroyed the village of Langtang, a Himalayan village in Nepal [10, 12, 13]. Fujita et al. [10] conducted field observations to determine the amount of avalanche deposits and rock debris resulting from these events. They estimated the deposit volumes of the primary and subsequent events as $6.81 \pm 1.54 \times 106$ and $0.84 \pm 0.92 \times 106$ m^3, respectively, by analyzing the difference between DEMs obtained from satellite data before the avalanche and helicopter- and UAV-based photogrammetric survey data collected after the event. In addition, they operated multiple UAVs to collect data during in situ observations. These data contribute not only to disaster records, but also to detailed case analyses and long-term assessments of avalanche deposits. Therefore, this study assessed the performance of multiple DEMs created from three cameras on board different UAVs and quantified the feasibility of low-cost photogrammetry in the high-elevation Himalayas through surveys conducted over Langtang Village in Nepal.

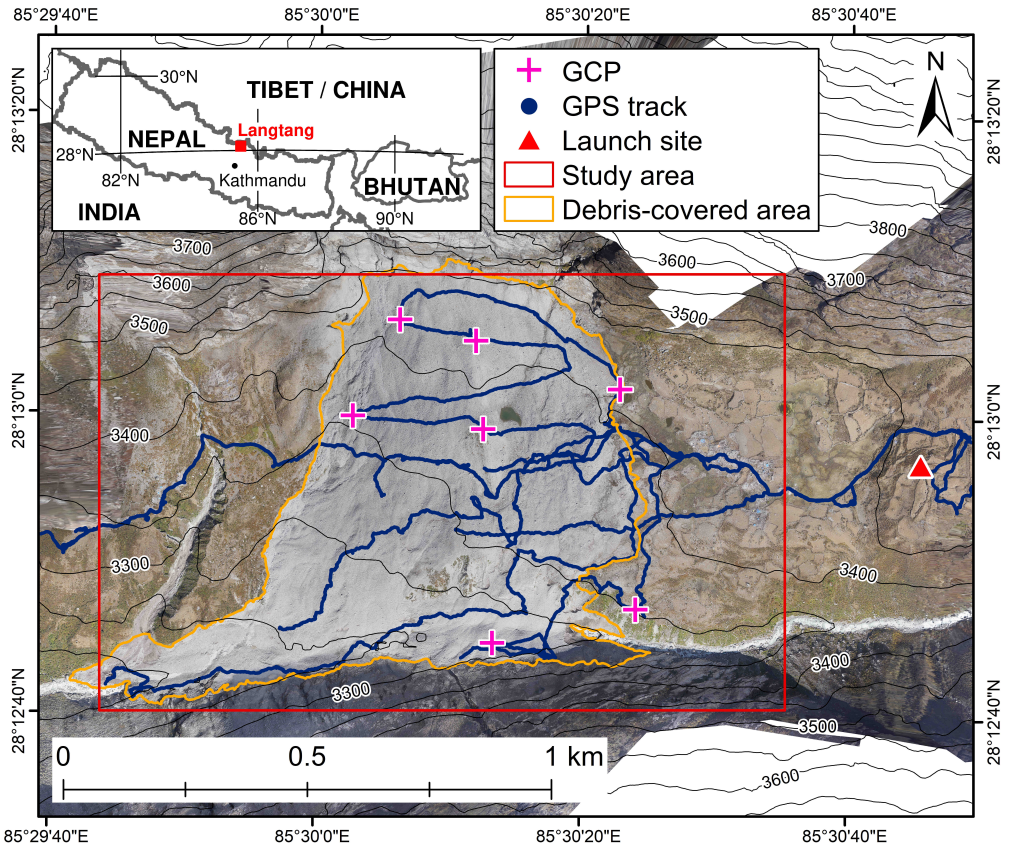

Fig. 1. Overview of the study area, Langtang Valley, Nepal. Orange and red polygons, blue circles, pink crosses, and the red triangle denote areas for debris-covered and DEM comparison, dGPS track, ground control points, and the launch site of UAVs, respectively. Background images are the orthoimage generated by Sony α7R (PA7) in this study. Contour lines derived from the High Mountain Asia 8 m DEM [14]. The inset map indicates the location of study area (red square).

2. Study Site, Data and Methodology

2.1. Study Site

Field observations were conducted at Langtang Village (28° 13'N, 85°30′E) located in Langtang Valley, Nepal Himalayas (**Fig. 1**), from October 23 to 25, 2015. The survey area was approximately 1.5 km (east to west) × 1.0 km (north to south), and the elevation ranged from 3170–3640 m above the ellipsoid. The village was destroyed by snow and ice avalanches induced by the 2015 Gorkha earthquake [10, 12, 13, 15] and was covered with large amounts of ice and rock debris. The surface of the debris-covered area was similar to that of typical Himalayan debris-covered glaciers. The Langtang River, the main river in the Langtang Valley, flows from east to west in the study area.

2.2. Differential GPS Measurement

We used a differential global positioning system (dGPS) (GEM-1 and 2, Enabler, Inc., and R10, Nikon-Trimble Co., Ltd.) to obtain ground control points (GCPs) and validation data for the UAV-DEMs in the study area. Details of the dGPS survey have been described previously by Fujita et al. [10]. A GPS base station was set at a hill (28.215°N, 85.520°E), approximately 2.4 km east of the survey area, and two other receivers were used for roving in kinematic mode with a logging interval of 1 s (**Fig. 1**). The geodetic accuracy of the dGPS system was evaluated to be less than 0.2 m both horizontally and vertically [9, 16]. We placed seven orange fabric sheets (1 m × 1 m) on the debris-covered area, which were collected using a dGPS survey to obtain precise positions for the use of GCPs (**Fig. 1**). The GPS data were post-processed using the RTKLIB GPS software package.[1] The coordinates were converted to the Universal Transverse Mercator (UTM) projection, specifically UTM zone 46N, using the WGS84 reference system at an elevation above the ellipsoid (m; hereafter, elevations). The position of the base station was derived from the precise point positioning service.[2] We then derived a DEM (GPS-DEM hereafter) at 0.5 m resolution using the inverse distance weighting method [10]. Subsequently, grid cells with no GPS points were eliminated by applying the method described by Tshering and Fujita [16].

2.3. UAV Based Photogrammetry

Three different cameras on board the three UAVs were used for aerial photogrammetry (**Table 1**). A quadcopter

1. http://www.rtklib.com [Accessed December 9, 2023]
2. https://webapp.geod.nrcan.gc.ca/geod/tools-outils/ppp.php [Accessed December 9, 2023]

Table 1. Cameras and UAV characteristics and SfM parameters.

Product name	PA7	XGR	EIX
UAV	Prodrone PD4-NPL	X-5	SensFly eBee
Camera	Sony α7R	Ricoh GR	Canon IXUS 125HS
Camera weight [g]	585	245	135
Number of flights	6	2	1
Mean flight height [m]	390	251	279
Number of images	377	257	188
Image size [pixels]	7360 × 4912	4352 × 3264	4608 × 3456
Focal length [mm]*	35	28	24
GSD** [m]	0.05	0.06	0.07
SfM parameters			
Alignment accuracy	High	High	High
Quality for dense cloud	High	High	High
Surface type	Height field	Height field	Height field
DEM / orthoimages			
Source	Mesh	Mesh	Mesh
DEM/ortho resolution [m]	0.50/0.09	0.50/0.12	0.50/0.15
DEM size [pixels]	7343 × 4521	6202 × 2547	4461 × 3289
Ortho image size [pixels]	40788 × 25113	25836 × 10607	11269 × 8106

*Equivalent to 35-mm film camera.
**Ground sampling distance.

Fig. 2. UAVs used in this study. (a) PD4-NPL, (b) X5, and (c) eBee.

UAV named PD4-NPL was created for use at high elevations and is capable of approximately 15 min of flight at cruise speeds of ~57 km · h^{-1} (Prodrone Co., Ltd., Nagoya, Japan; **Fig. 2(a)**). Two fixed-wing UAVs, SkyWalker X-5 (self-made; **Fig. 1(b)**) and eBee (SensFly Co., Ltd., Lausanne, Switzerland; **Fig. 1(c)**), capable of approximately 50 min and 30 min flights at cruise speeds of ~60 km · h^{-1} and ~36 km · h^{-1}, respectively, were also used. PD4-NPL and X-5 were manually piloted during take-off and landing, but were flown in autopilot mode during the survey. The eBee was fully operated in autopilot mode from take-off to landing. All UAVs were launched from a hill located on the eastern side of the survey area (**Fig. 1**), and flight heights were set at approximately 250–390 m above the ground level. PD4-NPL was equipped with a Sony α7R, which has a 36.3 megapixel sensor (7360 × 4912 pixels; PA7 hereafter); X-5 was equipped with a Ricoh GR, which has a 14.2 megapixel sensor (4352 × 3264 pixels; XGR hereafter); and the eBee was equipped with a Canon IXUS 125HS, which has a 16 megapixel sensor (4608 × 3456 pixels; EIX hereafter), respectively. The lenses of all cameras have a fixed focal length, except for EIX, which has a focal length between 4.3 and 21.5 mm; thus, we fixed it to be 4.3 mm. PA7 and XGR were set in time-lapse mode with a 1-s interval whereas EIX automatically released the shutter using the UAV autopilot system. Image overlap and sidelap for each UAV flight were set as 70% and 60%, respectively (**Fig. 3**). All images were captured in JPEG format and used for the SfM computation.

2.4. DEM and Orthoimages Creation

We utilized SfM photogrammetry software (Agisoft Photoscan Professional Version 1.0.3) to generate three DEMs and orthoimages following the common workflow of SfM processes [17–20]. The key parameters used in the software and related information are listed in **Table 1**. We processed 377, 257, and 188 images acquired using PA7, XGR, and EIX, respectively, to generate the sparse

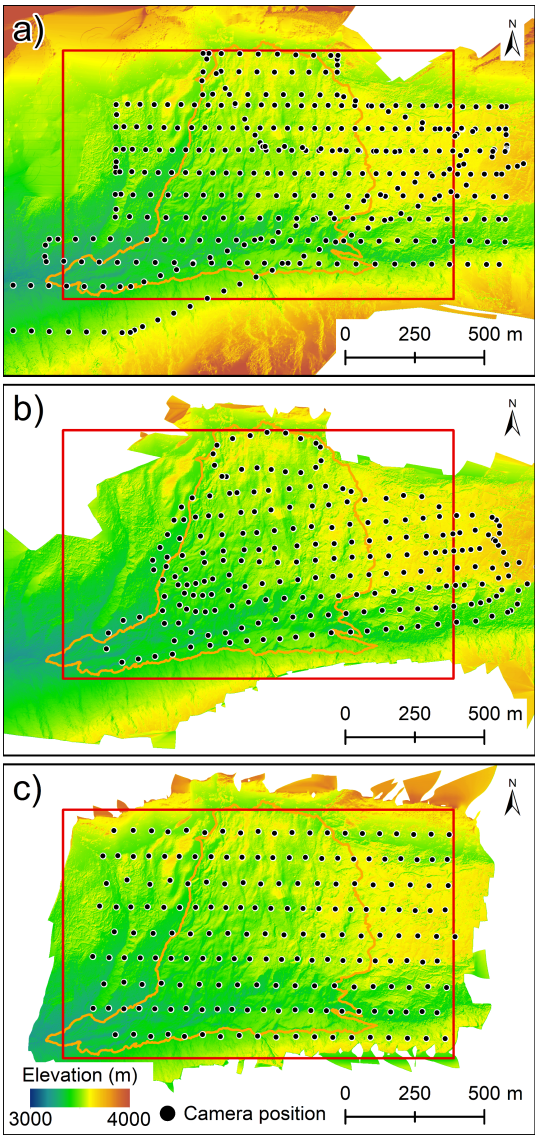

Fig. 3. Digital elevation models (DEMs) derived from (a) PA7, (b) XGR, and (c) EIX, with the camera position (black circles) indicated.

point clouds. The key and tie-point limits for the sparse point clouds were set to 40000 and 1000, respectively, to avoid the creation of less accurate points and reduce calculation time. We manually added seven GCPs during the process to georeference the sparse point clouds and generate dense point clouds. At each stage of the workflow, a high-accuracy setting was selected to reduce the calculation time. All three DEMs and ortho images were then derived with 0.5 m and the original resolutions, respectively (**Table 1**).

The analysis domains of the generated DEMs and orthoimages were determined by selecting an overlapping area for each product and ensuring that at least two images covered each location for each photogrammetric survey. We then assessed the accuracy of the photographic-based DEMs by comparing the elevation differences with the GPS-DEM, assuming that the GPS-DEM was accurate throughout the analysis domain.

3. Results

Figure 4 shows the accuracy of the three DEMs by comparing the elevation differences with those of the GPS-DEM. Means (dZ) and standard deviations (std dev.) of PA7-, XGR-, and EIX-DEMs are 0.10 ± 0.33, 0.13 ± 0.33, and -0.10 ± 0.39 m, respectively. Although the UAVs and the number of images for the DEM were different, dZ and std dev. for the three DEMs exhibited similar values. To evaluate the topographic effects on DEM quality, the elevation differences between the three DEMs and GPS-DEM were compared at every 25-m elevation and 5° slope interval (**Figs. 5(a)–(f)**). The root mean square errors (RMSEs) of the three DEMs were relatively large at lower elevations (~3250 m) downstream of the Langtang River and decreased with increasing elevation. A similar trend is observed in **Fig. 5(b)**, which shows dZ and std dev. The std dev. for each elevation band was $\sim\pm0.61$ m for all DEMs to an elevation of ~3350 m. Seventy percent of the comparison data were concentrated at 3350–3425 m, where RMSE and std dev. were small ($\sim\pm0.34$ m, **Figs. 5(a)** and **(b)**). **Figs. 5(d)** and **(e)** demonstrate that the RMSE and std dev. values increased proportionally with the slope, particularly when it exceeded 25°. The RMSE values for each DEM range from 0.27 to 0.43 m for slope angles below 25° and reach a maximum of ~0.86 m for angles greater than 25°. Only 5% of the grids in each DEM and GPS-DEM comparison had slope angles greater than 25°. The spatial distribution of elevation differences between all three DEMs and the GPS-DEM revealed that larger differences ($\sim\pm2.00$ m) were distributed in the southern and western part of the study area, particularly for the XGR- and EIX-DEMs (**Figs. 6(a)–(c)**). In addition, the EIX-DEM showed increasing elevation differences toward its eastern periphery.

4. Discussions

Our error evaluation results revealed larger differences at low elevations (~3250 m), steep slopes (25°<), and in the southern-to-western part of the comparison area. The increased vertical distance between the UAVs and the terrain surface could have caused a relatively larger RMSE downstream of Langtang River, where the altitude is low. In addition, studies using satellite-based DEMs have often reported increased vertical errors in steep terrains [21, 22], as yielded by our results. The more significant differences in elevation between the southern and western parts of the area can be explained by the lack of photogrammetric coverage owing to individual UAV flight routes and a limited GCP network. X-5 with GR mainly flew around the debris-covered area and did not completely cover the study area, whereas PD4-NPL with α7R and eBee with IXUS were operated over the entire study area (**Fig. 3**). In addition, because the flying speed was uncontrollable, X-5 circled widely around the corners with an inclined airframe attitude, which could have resulted in reduced overlap in the images around corners. The surface terrain of the western

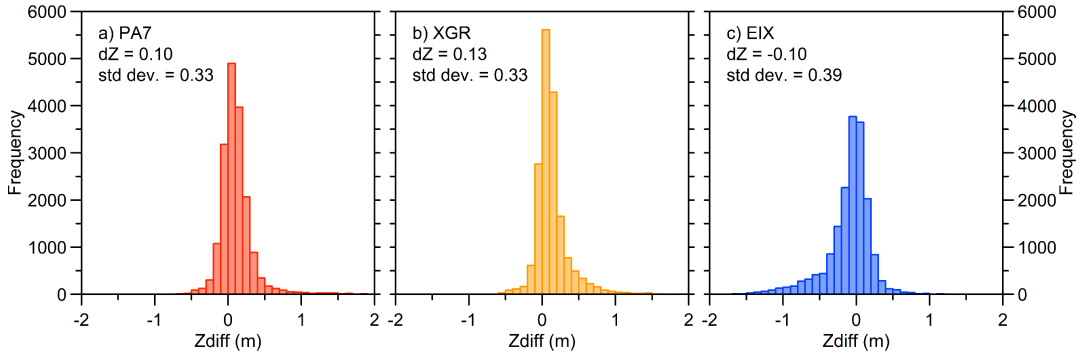

Fig. 4. Histograms displaying the elevation differences (*Z*diff) between each DEM and GPS-DEM. *dZ* and std dev. in each panel indicate the mean and standard deviation.

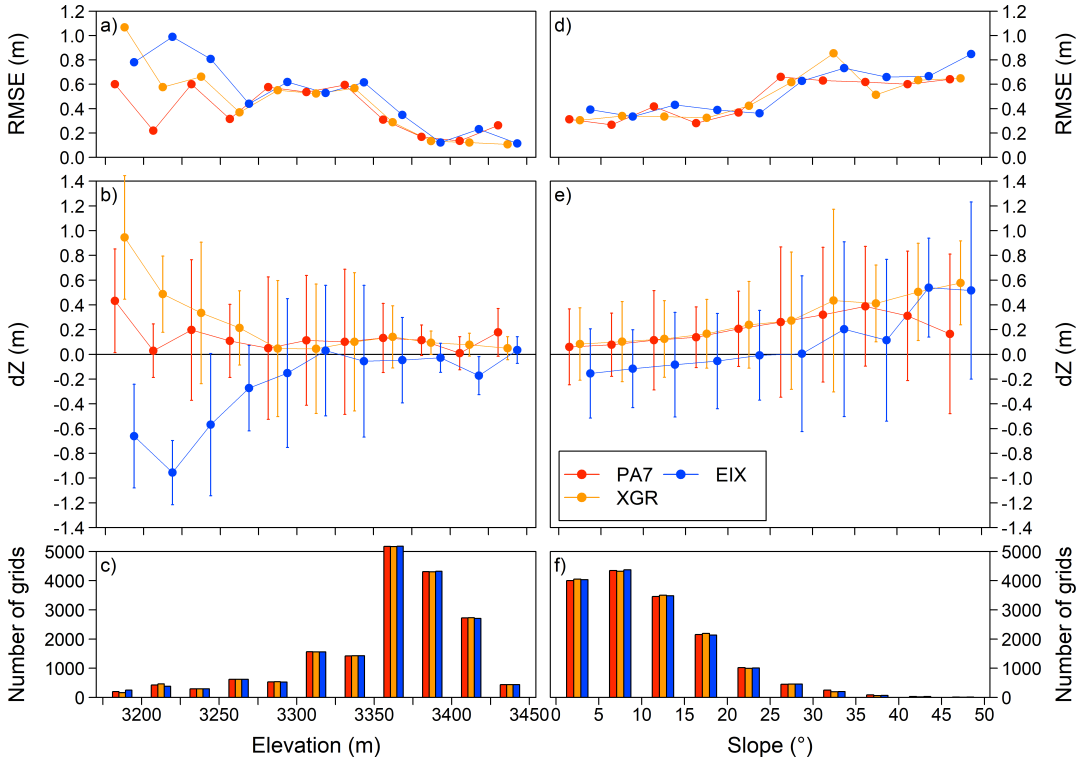

Fig. 5. Elevation differences between each DEM and GPS-DEM along altitude (left, a–c) and slope (right, d–f) with an interval of 25 m and 5°. (a, d) root mean square errors (RMSEs), (b, e) mean (*dZ*) and standard deviation (bars), and (c, f) number of grid cells are depicted.

part is relatively complicated and is located at lower elevations, which causes greater height differences between the UAVs and the ground. Thus, these factors induce a larger elevation difference in the XGR-DEM. Furthermore, using nadir images from UAV-based photogrammetry could have caused the doming error or dome effect [3], which is common in SfM-DEM [23, 24]. The EIX-DEM showed a positive bias in the central region and a depression in the eastern, southern, and western peripheries (**Fig. 6(c)**), suggesting that the dome error could affect the DEM quality. An adequate GCP network is one of approaches that mitigates doming errors, as mentioned in several studies [3, 23, 25]. Therefore, fewer GCPs, particularly around the western periphery, enhanced the elevation difference in the EIX-DEMs. Dome effects potentially affect the accuracy of PA7 and XGR-DEM, although this could not be confirmed from the spatial distribution of the errors.

Understanding how changes in the number of GCPs influence the DEM accuracy is crucial for improving its reliability. Gindraux et al. [23] generated multiple DEMs with varying numbers and placement of GCPs over three glaciers in the Swiss Alps. They then compared the vertical and horizontal accuracies of these DEMs with the results of dGPS observations, empirically deriving the relationship between the number of GCPs and the DEM accuracy as follows:

$$\sigma = a + \exp\left(-b \cdot \rho_{GCP}\right) + c, \quad \ldots\ldots\ldots \quad (1)$$

where σ represents the estimated vertical error of the DEM [m], ρ_{GCP} is the density of GCPs in the target

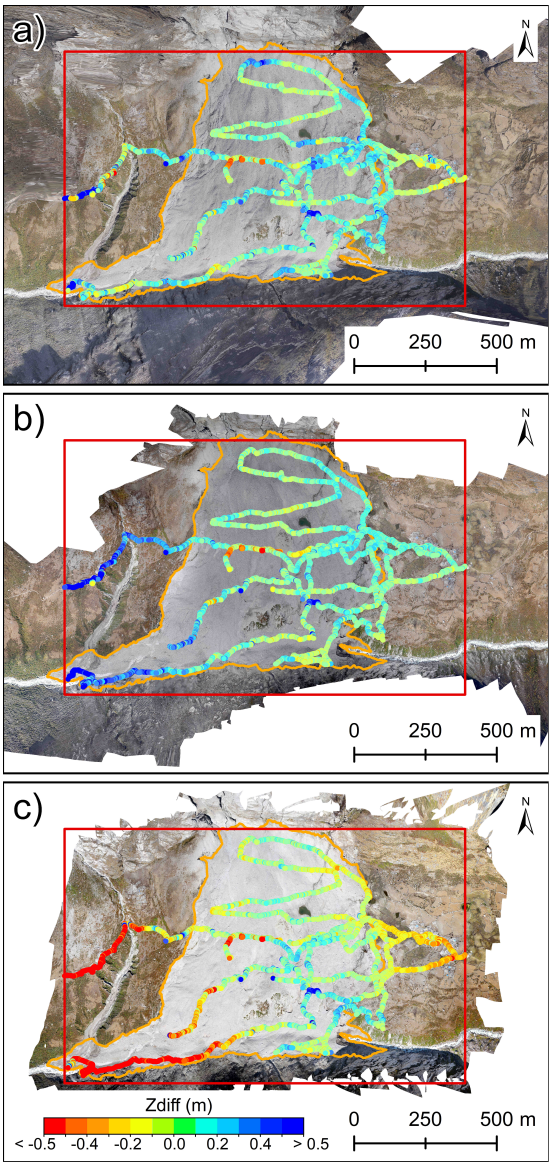

Fig. 6. Spatial distribution of elevation differences for each DEM against the GPS-DEM with (a) PA7, (b) XGR, and (c) EIX. The background images in (a)–(c) are the orthoimages generated by PA7, XGR and EIX, respectively.

area [1/km^2], and a, b, and c are coefficients. Gindraux et al. [23] set $a = 2.08$, $b = 0.59$, and $c = 0.17$. As the target region and GSD differ, these three parameters are expected to differ. However, if we calculate the GCP density based on the number of GCPs in this study and the comparison area (1.26 km^2) and apply this equation, σ would be ±0.25 m. When the number of GCPs is changed by ±2 (5 or 9), σ varies by approximately −19% to +22% depending on the number of GCPs. This means that, using PA7 from this study as an example, changing the number of GCPs by ±2 is estimated to result in a variation in the DEM accuracy of approximately ±0.27 m to ±0.40 m.

Many studies have used the UAV-SfM approach to generate DEMs with GCP, and their accuracies (RMSE and std dev.) fell between ±0.09 m to ±0.40 m, despite differences in resolution and methods of accuracy assessments for DEMs [6, 23, 26–29]. The accuracies of the DEMs in this study are equivalent to those obtained in previous studies; however, the errors are smaller than those of satellite-based DEMs [30]. In addition, our DEMs covered the full range of debris deposits in the study area and their qualities were feasible for hazard assessment, thus fulfilling the primary purpose of the survey.

At high elevations, such as in the Himalayas, the power consumption of UAV is a considerable constraint owing to the effects of cold conditions on the battery, and the difficulty of securing power sources. In addition, the power consumption of UAV is essential for logistics and related costs, which are not always required for operations in easily accessible areas. We utilized two types of UAVs, quadcopter and fixed-wing UAVs, and recognized that fixed-wing UAVs were better for comprehensive coverage because of their lower battery consumption. The X-5 with GR and PD4-NPL with α7R, for example, are powered by one (11.1 V, 4200 mAh, 0.31 kg) and two (22.2 V, 6000 mAh, 0.88 kg per battery) lithium-polymer batteries, respectively. The battery consumption of X-5 (56 W) was two orders of magnitude lower than that of PD4-NPL (1066 W). Moreover, to cover the survey area, the number of X-5 flights (twice, approximately 12 min per flight) was one-sixth that of PD4-NPL (six times, 14 min per flight). This difference suggests that, even if the cruise speeds of X-5 and PD4-NPL are considered, the fixed-wing UAV is appropriate for aerial photogrammetric surveys because of the smaller number of flights and longer flight time; thus, it consumes less power than the quadcopter. One of the notable characteristics of the PD4-NPL is its camera-mountable capacity. The α7R with a 35-mm lens weighs 585 g, which is heavier than GR (245 g) or IXUS (135 g). The α7R can provide the highest resolution images among the cameras used in this study and enables generation of DEM with reputable accuracy.

5. Conclusions

We conducted field observations and analyzed multiple DEMs obtained using different UAVs photogrammetry in Langtang Valley, Nepal. The SfM approach was used to produce three high-resolution DEMs (0.5 m). All DEMs were compared with a DEM from a dGPS survey conducted simultaneously with the UAV campaign. The three DEMs (PA7, XGR, and EIX) show that the elevation differences between each DEM and GPS-DEM range from −0.10 to +0.13 m for the mean and from 0.33 to 0.39 m for the standard deviation, respectively. The analysis of elevation changes based on slope and elevation, along with the spatial distribution, revealed that the errors were more pronounced at lower elevations (~3250 m), steeper slopes (>25°), and on the southern and western sides of each DEM. The main causes of the elevation differences were the sparse GCP network, lack of photogrammetric coverage, and large distance between the UAVs and the ground. The potential impact of errors must be considered

when using the DEMs produced in this study for future research. Nonetheless, our DEMs exhibited accuracies similar to those of other studies that utilized UAV-SfM techniques to generate DEMs, which are sufficient for hazard assessments. The precise DEM and orthorectified image data obtained and analyzed in this study are valuable disaster record data and are expected to contribute to research on long-term debris deposits and land use changes in Lantang Village.

Data Availability

The DEMs and orthoimages generated in this study are available online (https://doi.org/10.5281/zenodo.12799007).

Acknowledgments

We would like to thank the Department of Hydrology and Meteorology, Nepal, for providing the opportunity and permission to conduct field observations. We are indebted to Guide For All Seasons for its logistical support and to Prodrone Co., Ltd. for its dedicated support of the UAVs. This study was supported by J-RAPID of the Japan Science and Technology Agency, JSPS KAKENHI, grant numbers 26257202 and 26241020, and the Inoue Fund for Field Science of the Japanese Society of Snow and Ice. The work of W. Immerzeel was supported by funding from the European Research Council (ERC) under the European Union's Horizon 2020 research and innovation program (Grant Agreement No.676819).

References:

[1] M. J. Westoby, J. Brasington, N. F. Glasser, M. J. Hambrey, and J. M. Reynolds, "'Structure-from-Motion' photogrammetry: A low-cost, effective tool for geoscience applications," Geomorphology, Vol.179, pp. 300-314, 2012. https://doi.org/10.1016/j.geomorph.2012.08.021

[2] M. R. James and S. Robson, "Straightforward reconstruction of 3D surfaces and topography with a camera: Accuracy and geoscience application," J. of Geophysical Research: Earth Surface, Vol.117, Issue F3, Article No.F03017, 2012. https://doi.org/10.1029/2011JF002289

[3] M. R. James and S. Robson, "Mitigating systematic error in topographic models derived from UAV and ground-based image networks," Earth Surface Processes and Landforms, Vol.39, Issue 10, pp. 1413-1420, 2014. https://doi.org/10.1002/esp.3609

[4] L. Javernick, J. Brasington, and B. Caruso, "Modeling the topography of shallow braided rivers using structure-from-motion photogrammetry," Geomorphology, Vol.213, pp. 166-182, 2014. https://doi.org/10.1016/j.geomorph.2014.01.006

[5] M. W. Smith, J. L. Carrivick, and D. J. Quincey, "Structure from motion photogrammetry in physical geography," Progress in Physical Geography: Earth and Environment, Vol.40, No.2, pp. 247-275, 2015. https://doi.org/10.1177/0309133315615805

[6] W. W. Immerzeel, P. D. A. Kraaijenbrink, J. M. Shea, A. B. Shrestha, F. Pellicciotti, M. F. P. Bierkens, and S. M. de Jong, "High-resolution monitoring of Himalayan glacier dynamics using unmanned aerial vehicles," Remote Sensing of Environment, Vol.150, pp. 93-103, 2014. https://doi.org/10.1016/j.rse.2014.04.025

[7] P. Kraaijenbrink, S. W. Meijer, J. M. Shea, F. Pellicciotti, S. M. de Jong, and W. W. Immerzeel, "Seasonal surface velocities of a Himalayan glacier derived by automated correlation of unmanned aerial vehicle imagery," Annals of Glaciology, Vol.57, Issue 71, pp. 103-113, 2016. https://doi.org/10.3189/2016AoG71A072

[8] P. D. A. Kraaijenbrink, J. M. Shea, M. Litt, J. F. Steiner, D. Treichler, I. Koch, and W. W. Immerzeel, "Mapping surface temperatures on a debris-covered glacier with an unmanned aerial vehicle," Frontiers in Earth Science, Vol.6, Article No.64, 2018. https://doi.org/10.3389/feart.2018.00064

[9] C. Vincent, P. Wagnon, J. M. Shea, W. W. Immerzeel, P. Kraaijenbrink, D. Shrestha, A. Soruco, Y. Arnaud, F. Brun, E. Berthier, and S. F. Sherpa, "Reduced melt on debris-covered glaciers: Investigations from Changri Nup glacier, Nepal," Cryosphere, Vol.10, Issue 4, pp. 1845-1858, 2016. https://doi.org/10.5194/tc-10-1845-2016

[10] K. Fujita, H. Inoue, T. Izumi, S. Yamaguchi, A. Sadakane, S. Sunako, K. Nishimura, W. W. Immerzeel, J. M. Shea, R. B. Kayastha, T. Sawagaki, D. F. Breashears, H. Yagi, and A. Sakai, "Anomalous winter-snow-amplified earthquake-induced disaster of the 2015 Langtang avalanche in Nepal," Natural Hazards and Earth System Sciences, Vol.17, Issue 5, pp. 749-764, 2017. https://doi.org/10.5194/nhess-17-749-2017

[11] C. Watson, J. Kargel, and B. Tiruwa, "UAV-Derived Himalayan topography: Hazard assessments and comparison with global DEM products," Drones, Vol.3, Issue 1, Article No.18, 2019. https://doi.org/10.3390/drones3010018

[12] J. S. Kargel et al., "Geomorphic and geologic controls of geohazards induced by Nepal's 2015 Gorkha earthquake," Science, Vol.351, Issue 6269, Article No.aac8353, 2016. https://doi.org/10.1126/science.aac8353

[13] P. Lacroix, "Landslides triggered by the Gorkha earthquake in the Langtang Valley, volumes and initiation processes," Earth, Planets and Space, Vol.68, Article No.46, 2016. https://doi.org/10.1186/s40623-016-0423-3

[14] D. Shean, "High mountain Asia 8-meter DEM mosaics derived from optical imagery, version 1," [Data Set], NASA National Snow and Ice Data Center Distributed Active Archive Center, 2017. https://doi.org/10.5067/KXOVQ9L172S2

[15] H. Nagai, M. Watanabe, N. Tomii, T. Tadono, and S. Suzuki, "Multiple remote-sensing assessment of the catastrophic collapse in Langtang Valley induced by the 2015 Gorkha earthquake," Natural Hazards and Earth System Sciences, Vol.17, Issue 11, pp. 1907-1921, 2017. https://doi.org/10.5194/nhess-17-1907-2017

[16] P. Tshering and K. Fujita, "First in situ record of decadal glacier mass balance (2003–2014) from the Bhutan Himalaya," Annals of Glaciology, Vol.57, No.71, pp. 289-294, 2016. https://doi.org/10.3189/2016aog71a036

[17] Agisoft LLC, "PhotoScan User Manual, Professional Edition, Version 1.0.0," 2013.

[18] A. Lucieer, S. M. de Jong, and D. Turner, "Mapping landslide displacements using structure from motion (SfM) and image correlation of multi-temporal UAV photography," Progress in Physical Geography: Earth and Environment, Vol.38, No.1, pp. 97-116, 2014. https://doi.org/10.1177/0309133313515293

[19] M. J. Westoby, S. A. Dunning, J. Woodward, A. S. Hein, S. M. Marrero, K. Winter, and D. E. Sugden, "Instruments and methods: Sedimentological characterization of Antarctic moraines using UAVs and structure-from-motion photogrammetry," J. of Glaciology, Vol.61, Issue 230, pp. 1088-1102, 2015. https://doi.org/10.3189/2015JoG15J086

[20] M. W. Ewertowski, A. M. Tomczyk, D. J. A. Evans, D. H. Roberts, and W. Ewertowski, "Operational framework for rapid, very-high resolution mapping of glacial geomorphology using low-cost unmanned aerial vehicles and structure-from-motion approach," Remote Sensing, Vol.11, No.1, Article No.65, 2019. https://doi.org/10.3390/rs11010065

[21] K. Fujita, R. Suzuki, T. Nuimura, and A. Sakai, "Performance of ASTER and SRTM DEMs, and their potential for assessing glacial lakes in the Lunana region, Bhutan Himalaya," J. of Glaciology, Vol.54, No.185, pp. 220-228, 2008. https://doi.org/10.3189/002214308784886162

[22] T. Nuimura, K. Fujita, S. Yamaguchi, and R. R. Sharma, "Elevation changes of glaciers revealed by multitemporal digital elevation models calibrated by GPS survey in the Khumbu region, Nepal Himalaya, 1992–2008," J. of Glaciology, Vol.58, No.210, pp. 648-656, 2012. https://doi.org/10.3189/2012jog11j061

[23] S. Gindraux, R. Boesch, and D. Farinotti, "Accuracy assessment of digital surface models from unmanned aerial vehicles' Imagery on Glaciers," Remote Sensing, Vol.9, Issue 2, Article No.9, 2017. https://doi.org/10.3390/rs9020186

[24] L. Girod, C. Nuth, A. Kaäb, B. Etzelmüller, and J. Kohler, "Terrain changes from images acquired on opportunistic flights by SfM photogrammetry," Cryosphere, Vol.11, No.2, pp. 827-840, 2017. https://doi.org/10.5194/tc-11-827-2017

[25] T. N. Tonkin and N. G. Midgley, "Ground-control networks for image based surface reconstruction: An investigation of optimum survey designs using UAV derived imagery and structure-from-motion photogrammetry," Remote Sensing, Vol.8, No.9, Article No.786, 2016. https://doi.org/10.3390/rs8090786

[26] J. Goetz and A. Brenning, "Quantifying uncertainties in snow depth mapping from structure from motion photogrammetry in an Alpine area," Water Resource Research, Vol.55, No.9, pp. 7772-7783, 2019. https://doi.org/10.1029/2019WR025251

[27] F. Clapuyt, V. Vanacker, and K. Van Oost, "Reproducibility of UAV-based earth topography reconstructions based on structure-from-motion algorithms," Geomorphology, Vol.260, pp. 4-15, 2016. https://doi.org/10.1016/j.geomorph.2015.05.011

[28] W. Yang, C. Zhao, M. Westoby, T. Yao, Y. Wang, F. Pellicciotti, J. Zhou, Z. He, and E. Miles, "Seasonal dynamics of a temperate Tibetan glacier revealed by high-resolution UAV photogrammetry and in situ measurements," Remote Sensing, Vol.12, No.15, Article No.2389, 2020. https://doi.org/10.3390/RS12152389

[29] S. Sunako, K. Fujita, T. Izumi, S. Yamaguchi, A. Sakai, and R. B. Kayastha, "Up-glacier propagation of surface lowering of Yala glacier, Langtang valley, Nepal Himalaya," J. of Glaciology, Vol.69, No.274, pp. 425-432, 2023. https://doi.org/10.1017/jog.2022.118

[30] E. Berthier, C. Vincent, E. Magnússon, Á. Þ. Gunnlaugsson, P. Pitte, E. Le Meur, M. Masiokas, L. Ruiz, F. Pálsson, J. M. C. Belart, and P. Wagnon, "Glacier topography and elevation changes derived from Pléiades sub-meter stereo images," Cryosphere, Vol.8, No.6, pp. 2275-2291, 2014. https://doi.org/10.5194/tc-8-2275-2014

Name:
Sojiro Sunako

ORCID:
0000-0002-0403-1950
Affiliation:
Research Fellow, Snow and Ice Research Center, National Research Institute for Earth Science and Disaster Resilience (NIED)
Address:
187-16 Maeyama, Suyoshi, Nagaoka, Niigata 940-0821, Japan
Brief Career:
2019- Snow and Ice Research Center, NIED
Selected Publications:
• "Up-glacier propagation of surface lowering of Yala Glacier, Langtang Valley, Nepal Himalaya," J. of Glaciology, Vol.69, Issue 274, pp. 425-432, 2023
Academic Societies & Scientific Organizations:
• The Japanese Society of Snow and Ice
• Japan Geoscience Union (JpGU)
• International Glaciological Society (IGS)

Name:
Koji Fujita

ORCID:
0000-0003-3753-4981
Affiliation:
Professor, Graduate School of Environmental Studies, Nagoya University
Address:
D2-1(510), Furo-cho, Chikusa-ku, Nagoya, Aichi 464-8601, Japan
Brief Career:
1992- Nagoya University
Selected Publications:
• "Modelling the development and decay of cryoconite holes in northwestern Greenland," The Cryosphere, Vol.17, Issue 8, pp. 3309-3328, 2023
• "Physically based summer temperature reconstruction from melt layers in ice cores," Earth and Space Science, Vol.8, Issue 7, Article No.e2020EA001590, 2021.
Academic Societies & Scientific Organizations:
• International Glaciological Society (IGS)
• European Geosciences Union (EGU)
• American Geophysical Union (AGU)
• Japan Geoscience Union (JpGU)
• The Japanese Society of Snow and Ice

Name:
Satoru Yamaguchi

ORCID:
0000-0001-9972-0443
Affiliation:
Principal Researcher, Snow and Ice Research Center, National Research Institute for Earth Science and Disaster Resilience (NIED)
Address:
187-16 Maeyama, Suyoshi, Nagaoka, Niigata 940-0821, Japan
Brief Career:
2002- Snow and Ice Research Center, NIED
Selected Publications:
• "A Novel Method to Visualize Liquid Distribution in Snow: Superimposition of MRI and X-ray CT Images," Annals of Glaciology, 2023.
Academic Societies & Scientific Organizations:
• The Japanese Society of Snow and Ice
• International Glaciological Society (IGS)

Name:
Hiroshi Inoue

Affiliation:
Visiting Researcher, National Research Institute for Earth Science and Disaster Resilience (NIED)
Address:
3-1 Tennodai, Tsukuba, Ibaraki 305-0006, Japan
Brief Career:
1988-1996 IISEE, Building Research Institute
1996-2021 NIED
2021- Visiting Researcher, NIED
2021- Researcher, Disaster Prevention Research Institute, Kyoto University
Selected Publications:
• "Waveform inversion in the frequency domain for the simultaneous determination of earthquake source mechanism and moment function," Geophysical J. Int., Vol.173, Issue 3, pp. 1000-1011, 2008.
• "Multicopter aerial photography for natural disaster research," Report of the National Research Institute for Earth Science and Disaster Prevention, No.81, pp. 61-98, 2014.
• "Development of seismic intensity meter for the Philippines, J. Disaster Res., Vol.10, No.1, pp. 35-42, 2015.
Academic Societies & Scientific Organizations:
• Seismological Society of Japan (SSJ)
• Seismological Society of America (SSA)

Name:
Walter W. Immerzeel

ORCID:
0000-0002-2010-9543
Affiliation:
Professor, Faculty of Geosciences, Department of Physical Geography, Utrecht University
Address:
8a Princetonlaan, Utrecht 3584 CB, The Netherlands
Brief Career:
2008-2013 Utrecht University
2011-2014 ETH Zurich
2014- Utrecht University
Selected Publications:
• "Importance and vulnerability of the world's water towers," Nature, Vol.577, pp. 364-369, 2020.

Name:
Takeki Izumi

Affiliation:
Assistant Professor, School of Urban Environmental Sciences, Tokyo Metropolitan University
Address:
4-1-1 Minamiosawa, Hachioji, Tokyo 192-0397, Japan
Academic Societies & Scientific Organizations:
• The Association of Japanese Geographers (AJG)
• The City Planning Institute of Japan (CPIJ)
• The Japan Society of Civil Engineers (JSCE)
• The Meteorological Society of Japan (MSJ)
• Geographic Information System Association (GISA)

Name:
Rijan B. Kayastha

ORCID:
0000-0002-5896-1731
Affiliation:
Professor, Department of Environmental Science and Engineering, School of Science, Kathmandu University
Address:
University Road, Dhulikhel, Kathmandu 45200, Nepal
Brief Career:
2006- Kathmandu University
Selected Publications:
• "Glacial Lakes Outburst Floods (GLOFs) modelling of Thulagi and Lower Barun Glacial Lakes of Nepalese Himalaya," Progress in Disaster Science, Vol.7, Article No.100106, 2020.
Academic Societies & Scientific Organizations:
• International Glaciological Society (IGS)
• Society of Hydrologist and Meteorologist-Nepal (SOHAM-NEPAL)
• International Association of Hydrological Sciences (IAHS)